Enhanced Framework Rigidity of a Zeolitic Metal-Azolate via Ligand Substitution

Hongqiang Gao [1,†], Wenjuan Wei [2,†], Liyuan Dong [2], Guoqiang Feng [3,*], Xingxing Jiang [4,*], Rong Wu [1,*], Zheshuai Lin [4] and Wei Li [2]

[1] School of Physical Science and Technology, Xinjiang University, Urumqi 830046, China; ghqe1@outlook.com
[2] School of Physics, Huazhong University of Science and Technology, Wuhan 430074, China; wwenjuan@hust.edu.cn (W.W.); dongliyuan@hust.edu.cn (L.D.); wl276@hust.edu.cn (W.L.)
[3] Department of Physics and Mechanical & Electrical Engineering, Hubei University of Education, Wuhan 430205, China
[4] Technical Institute of Physics and Chemistry, Chinese Academy of Sciences, Beijing 100190, China; zslin@mail.ipc.ac.cn
* Correspondence: gqfeng627@hust.edu.cn (G.F.); xxjiang@mail.ipc.ac.cn (X.J.); wurongxju@sina.com (R.W.); Tel.: +86-27-8754-3755 (G.F.)
† These authors contributed equally to this work.

Abstract: The elastic properties of a zeolitic metal-azolate framework, $Zn(mtz)_2$ (MAF-7, $mtz^- = 3$-methyl-1,2,4-triazolate), have been examined from the view point of the first principles calculations and experiments. Our results demonstrate that the three independent elastic constants of MAF-7 are about 5.0–73.3% higher than those of ZIF-8, though they are isomorphic. The electron-donating effect of the nitrogen atom at the 2-position in mtz- ring dominantly accounts for such a prominent difference. The detailed analysis of the full elastic tensors reveals that the volume moduli, shear moduli, and Poisson's ratios of MAF-7 are about 3.4% to 20.1%, 3.2% to 20.6%, and −30.3% to 12.3% higher than those of ZIF-8. The underlying structural reasons were discussed to explain the anisotropic difference of those properties. Moreover, the conclusion deduced from first-principle calculations was also been verified by nanoindentation and high-pressure synchrotron X-ray diffraction measurements.

Keywords: zinc-triazolate framework; elastic constants; volume moduli; shear moduli; Poisson's ratios

1. Introduction

Zeolitic metal-azolate frameworks (MAFs), a subclass of porous MOFs, have been attracting particular attention due to their potential application [1] superior to traditional zeolites in many fields, such as gas storage/separation [2–4], catalysis [5], sensing, and drug delivery [6,7]. In practical application, the zeolitic MAFs would experience several rounds of mechanical manufacturing processes. To maintain the intrinsic properties of zeolitic MAFs during the mechanical manufacturing processes, their fundamental mechanical properties should be fully understood and, therefore, the study about the mechanical property has become one of the hottest topics in the field of MAF study. Recently, much study has revealed that significant difference exists between zeolitic MAFs and zeolites in terms of mechanical robustness [8–10]. In 2009, Moggach et al. performed high pressure single-crystal X-ray diffraction studies on (ZIF), $Zn(mim)_2$ (ZIF-8 [11], mim = 2-methylimidazolate), a zeolitic imidazolte framework, and discovered that the exertion of pressure can increase the accessible surface area and its absorption performance [12]. A follow-up high-pressure powder X-ray diffraction study reveals similar results and shows that the hydrostatic behavior of ZIF-8 also strongly depends on the

size of different pressuretransmitting mediums [13]. Recently, Tan et al. reported a comprehensive nanoindentation study of ZIFs, and accordingly elaborate the structure-property relationship of its mechanical property [14]. In 2012, their another work reports the anomalously shear modulus of ZIF-8 one order lower than that of zodalite in magnitude [15].

Nevertheless, all these studies focused on zeolitic imidazolate frameworks (ZIFs), and up to now the mechanical property of zeolitic triazolate frameworks have not been investigated yet. In this work, we present a systematic study on the elastic properties of a zeolitic triazolate, $Zn(mtz)_2$ (MAF-7 [16], mtz = 3-methyl-1,2,4-triazolate), which is isomorphous to ZIF-8. To examine the electronic difference in elastic properties between 2-methylimidazolate and 3-methyl-1,2,4-triazolate, we performed first-principles calculations to extract the full elastic tensors of the cubic MAF-7. Our density functional theory (DFT) results elucidated that, compared with ZIF-8, the trivial electron-donating effect strongly enhance the mechanical strength of MAF-7, especially in the ability to resist uniaxial and shear stresses. Moreover, the calculated result was also testified by nanoindentation and synchrotron high-pressure powder X-ray diffraction experiments.

2. Results and Discussion

MAF-7 is isomorphous to ZIF-8 and crystallizes in the same cubic space group *I*-43*m* as reported by Zhang et al. [16]. In the structure, the Zn^{2+} ion is tetrahedrally coordinated with the triazolate ligand to form $Zn(mtz)_2$ open framework with zeolitic sodalite (SOD) architecture. The mtz$^-$ ligand coordinates with the zinc ion via its N atoms on the 2- and 4-positions, and the N on the 1-position unbonded [16,17]. It should be emphasized the lone pair electrons of the unbonded nitrogen can donate electron to the adjacent N at the 2-position, and this effect pushes the lone pair electrons of the coordinated N to bonded with the zinc center more tightly (Figure 1). The experimentally-determined Zn-N bond length of MAF-7 (1.980(2) Å) is slightly shorter than that of ZIF-8(1.983(3) Å) at same temperature, confirming the stronger covalent interaction in the former than the latter [17].
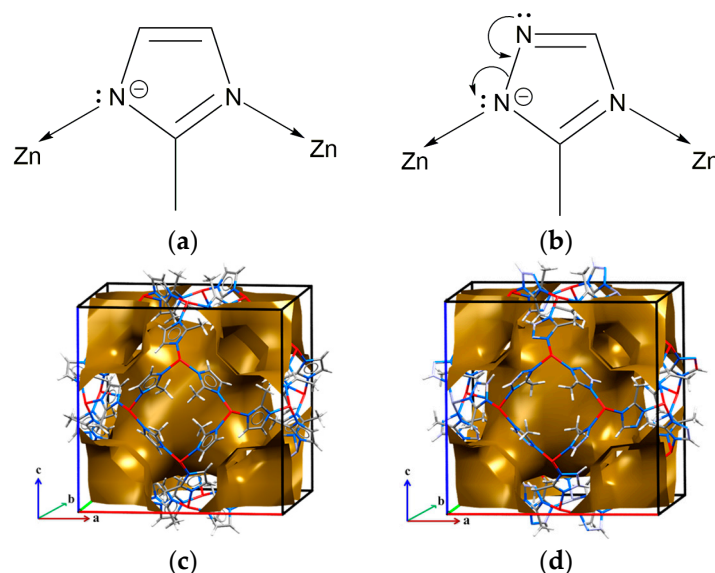

Figure 1. Crystal structures of ZIF-8 and MAF-7. Coordination modes of (**a**) imidazolate and (**b**) 1,2,4-triazolate; framework structures of (**c**) ZIF-8 and (**d**) MAF-7. The electron-donating effect is indicated by arrows. The yellow surfaces indicate the solvent accessible voids of ZIF-8 and MAF-7 which are 49.8% and 51.7%, respectively [16]. Color codes used: zinc, red; carbon, grey; nitrogen, blue; hydrogen, white.

The elastic properties of MAF-7 are listed in Table 1. Clearly, the calculated C_{ij}'s satisfy the fundamental elastic stability criteria for a cubic crystal, i.e., $C_{11} > |C_{12}|$, $C_{11} + 2C_{12} > 0$ and

$C_{44} > 0$ [18,19]. It is observed that the three independent elastic constants C_{11}, C_{12}, and C_{44}, which represent the stiffness of a cubic structure, are 5.0%, 15.8%, and 73.3% larger than those of ZIF-8, indicating the overall higher rigidity of MAF-7 than ZIF-8. The larger C_{12} and C_{44} values [20] of MAF-7 result in its significantly different elastic properties compared with ZIF-8 as we shall discuss below. To further understand the comprehensive elastic properties of MAF-7, we performed the full tensorial analysis of the elastic constants and extracted the key mechanical index (including anisotropic Young's moduli (*E*), shear moduli (*G*), and Poisson's ratios (*ν*), as listed in Table 1 and displayed in Figures 2–4) [21]. We will discuss them in details in the following sections.

Table 1. The elastic properties of MAF-7 and ZIF-8 extracted from DFT calculations.

| Elastic Properties	Framework	MAF-7	ZIF-8 [15]
Stiffness coefficient, C_{ij} **(GPa)**	C_{11}	11.587	11.038
	C_{12}	9.643	8.325
	C_{44}	1.635	0.943
Young's modulus, *E* **(GPa)**	E_{max}	$E(111) = 4.659$	$E(100) = 3.879$
		$E(110) = 4.009$	$E(110) = 2.953$
	E_{min}	$E(100) = 2.828$	$E(111) = 2.736$
Shear modulus, *G* **(GPa)**	G_{max}	1.64	1.36
	G_{min}	0.97	0.94
Poisson's ratio, *υ*	$υ_{max}$	$ν < 110, 001 > = 0.64$	$ν < 110, 1\bar{1}0 > = 0.57$
	$υ_{min}$	$ν < 110, 1\bar{1}0 > = 0.23$	$ν < 110, 001 > = 0.33$
Anisotropy measure	Zener, *A* (=1 if isotropic)	1.68	0.70
	E_{max}/E_{min}	1.65	1.42
Bulk modulus K(GPa)		10.29	9.23
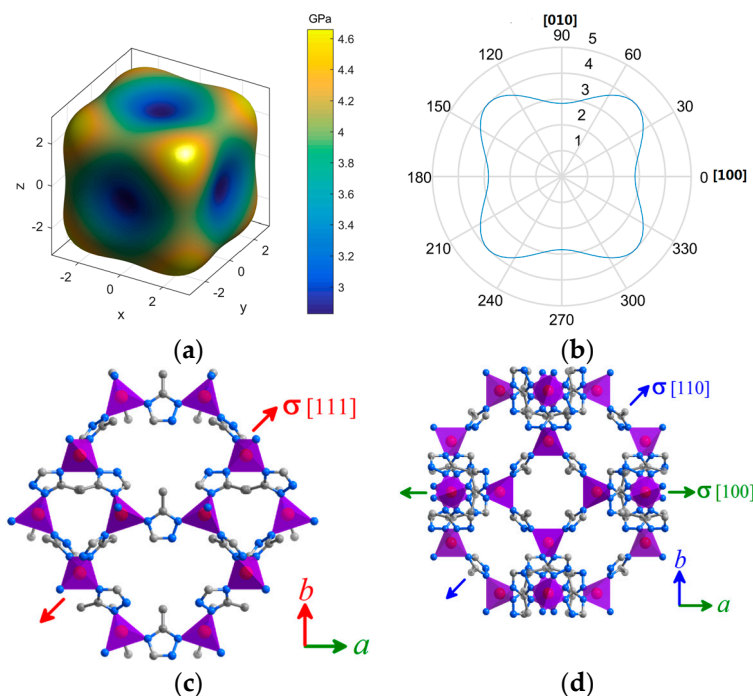
Figure 2. Young's modulus (*E*) representation surfaces. (**a**) 3D and (**b**) 2D surface extracted from the calculated elastic constants. (**c**,**d**) The schematic of stresses σ applied along [111], [110], [100] directions, corresponding to the maximum, intermediate, and minimum modulus.

We first focus on Young's modulus, which represents the stiffness with respect to uniaxial stress. The extracted $E_{(100)}$, $E_{(110)}$, and $E_{(111)}$ of MAF-7 are 2.828, 4.009, and 4.659 GPa, respectively. The representation 3D and 2D surfaces of E are shown in Figure 2a,b, which indicate that the Young's modulus exhibit strong spatial anisotropy. It can be seen that E reaches the maximum along the <111> direction, the body diagonal perpendicular to the SOD six-membered ring. The E surfaces exhibit subsidences along the cubic axes normal to the SOD four-membered ring, implying that the MAF-7 is mostly mechanical compliant along the <100> direction. It is notable that the directions of E_{max} and E_{min} of MAF-7 are reverse to those of ZIF-8. In an arbitrary direction [hkl], Young's modulus of a cubic system is given in terms of S_{ij}, $\{E_{[hkl]}\}^{-1} = S_{11} - (2S_{11} - 2S_{12} - S_{44})N^4$, where $N^4 = n_1^2 n_2^2 + n_1^2 n_3^2 + n_2^2 n_3^2$, n_1, n_2, n_3 are direction cosines for the direction [hkl] [19]. If $2S_{11} - 2S_{12} - S_{44} > 0$, E reaches the maximum and minimum in the <111> and <100> directions, as the case in MAF-7. On the contrary, if $2S_{11} - 2S_{12} - S_{44} < 0$, the reverse results would be obtained as in ZIF-8.

From Table 1, it is clear that the E_{max} and E_{min} of MAF-7 are about 20.1% and 3.4% higher than those of ZIF-8. Meanwhile, the E values of MAF-7 is more anisotropic than ZIF-8, characterized by the corresponding index $A_E = E_{max}/E_{min} = 1.65$, 16.2% higher than that of ZIF-8 (1.42). The remarkable difference in Young's modulus between MAF-7 and ZIF-8 originate from the aforementioned electron-donating effect. Such an effect leads to the stronger Zn-N bonds in MAF-7, which resultantly strengthens its resistance to axial deformation dominantly related with the change of Zn-N bonds and rotation of Zn-triazolate-Zn bond angles compared with ZIF-8 [15].

To testify the conclusion about calculated Young's modulus, we conducted nanoindentation experiments using non-desolvated single-crystals to extract the elastic moduli of MAF-7. The experiment was carried out in the quasi-static mode and the maximum load was set as 5000 μN. Representative load-indentation depth (P-h) curves obtained normal to the (100) and (110) faces are displayed in Figure 3. The smooth loading parts of both faces demonstrates that the plastic deformation occurs underneath the three-side pyramidal Berkovich tip during indentation and is relatively homogeneous in nature [22]. The average values of $E_{(100)}$ and $E_{(110)}$, extracted from the P-h curves, are 2.92(14) and 3.87(17) GPa, respectively. The good agreement between the calculated and observed values (with relative error less than 5%) confirms the high Young's modulus of MAF-7.
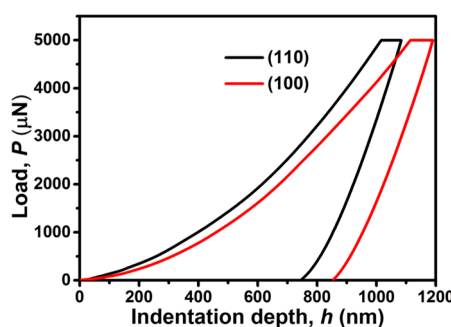
Figure 3. Representative load-indentation depth (P-h) curves of MAF-7 measured with a Berkovich tip normal to the (110) and (100) planes.

Now we turn attention to the shear modulus (G). Along an arbitrary direction [hkl], the general expression for shear modulus in cubic system is $\{G(hkl)\}^{-1} = S_{44} + 2(2S_{11} - 2S_{12} - S_{44})N^4$, in which the direction-dependent values also depends on N^4 [19]. The 3D representation G surface, characterized via the maximal and minimal G, is shown in Figure 4. Accordingly, the G_{max} and G_{min} are along the <100> and <110> directions, respectively, reversely to the situation in ZIF-8. As seen from Table 1, the G_{min} and G_{max} of MAF-7 are about 3.2% and 20.6% larger than those from ZIF-8, and the anisotropy in G of MAF-7 is about 15.9% higher than that of ZIF-8. For a cubic crystal, G_{max} (=C_{44}) characterize the ability to resist to shear strain on the (100) plane under a pair of opposing shear stresses τ exerted along the <0kl> directions, and $G_{min} = ((C_{11} - C_{12})/2)$ represents the resistance to shear on the (110)

plane under a shear along the <1–10> direction [23]. The framework of MAF-7 resists shear mostly through the cooperative bending of the N-Zn-N and rotation of Zn-mtz-Zn bond angles. Like ZIFs, MAF-7 features four-membered rings in the structure, which are most susceptible to distortion under antiparallel shear forces. For a rectangle, shearing the edges is easier than the diagonals. As such, the same pair of opposing shear stresses τ applied on the (100) or (110) plane can generate larger deformation along the <110> than <100> direction, hence, leading to G_{min} along <110> while G_{max} along <100> direction.
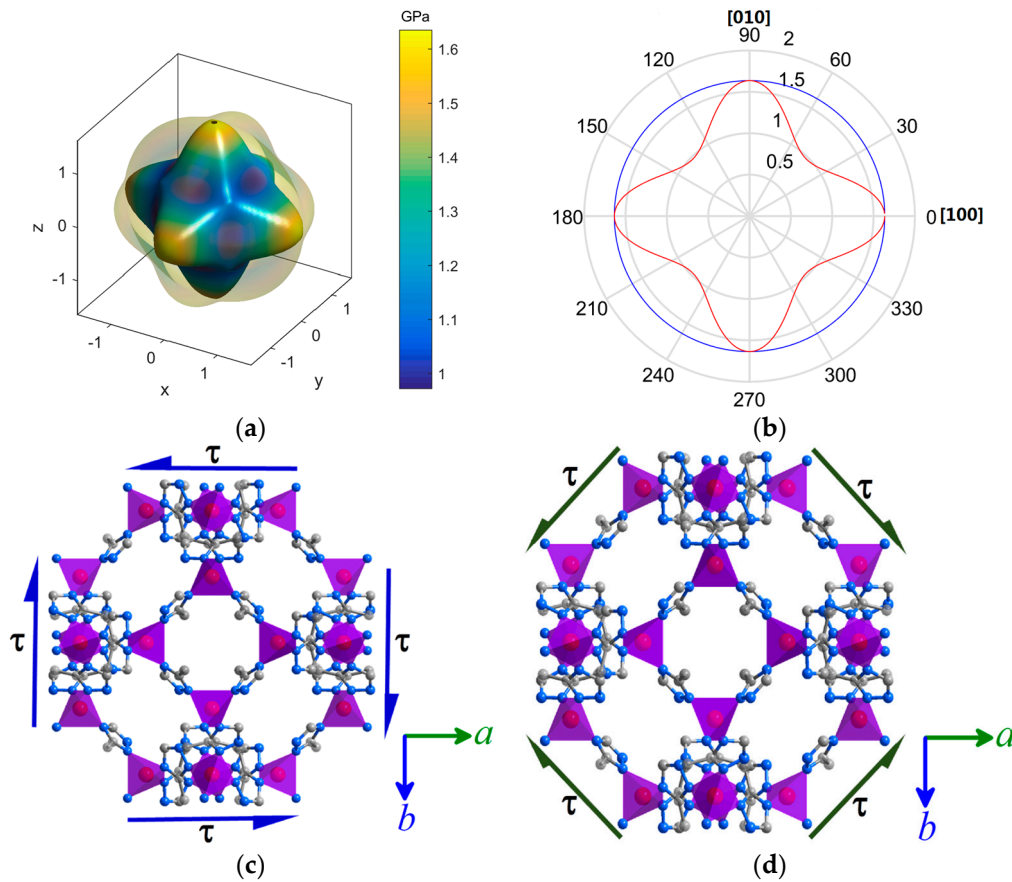

Figure 4. Shear modulus (G) representation surfaces. (**a**) 3D and (**b**) 2D surface based on the calculated elastic constants, The opposing shear stresses τ are applied (**c**) on the (100) planes along <0kl> directions and (**d**) on the (110) planes along <1$\bar{1}$0> directions, corresponding to the maximum and minimum shear modulus.

Now, we focus on the Poisson's ratio (ν) which is defined as the negative ratio of the transverse strain (ε_j) to the longitudinal strain (ε_i), i.e., $\nu = -\varepsilon_j/\varepsilon_i$ [24]. Poisson's ratio ν is expressed as $\nu[h'k'l'][hkl] = \frac{S_{12}+(S_{11}-S_{12}-S_{44}/2)M^4}{S_{11}-(2S_{11}-2S_{12}-S_{44})N^4}$ in a cubic system [19]. Therein, $M^4 = n_1^2 m_1^2 + n_2^2 m_2^2 + n_3^2 m_3^2$, where m_1, m_2, and m_3 are direction cosines for the direction [$h'k'l'$], respectively [19]. It can be seen that the directions of the ν_{max} and ν_{min} of MAF-7 are also closely related with the direction-dependent value of M^4 and N^4. The representation surfaces for Poisson's ratios of MAF-7 are shown in Figure 5a,b, and the maximum and minimum ν values are 0.23 and 0.64 along <1$\bar{1}$0> and <001> directions. As illustrated in Figure 5c, when the structure is elongated along the <110> propelled by axial strain, ν_{min} and ν_{max} are obtained along the <001> and <1$\bar{1}$0>, respectively. The ν_{max} is 12.3% higher while the ν_{min} is 30.3% lower than ZIF-8. The large ν_{max} of MAF-7 coincide with its high shear modulus, which arises from the electron-donating effect as well. However, the much lower ν_{min} of MAF-7

than ZIF-8 implies that such an electron effect also negatively contribute to the framework stability enhancement under axial tensile or compression stresses along some directions.


(a)

(b)

(c)
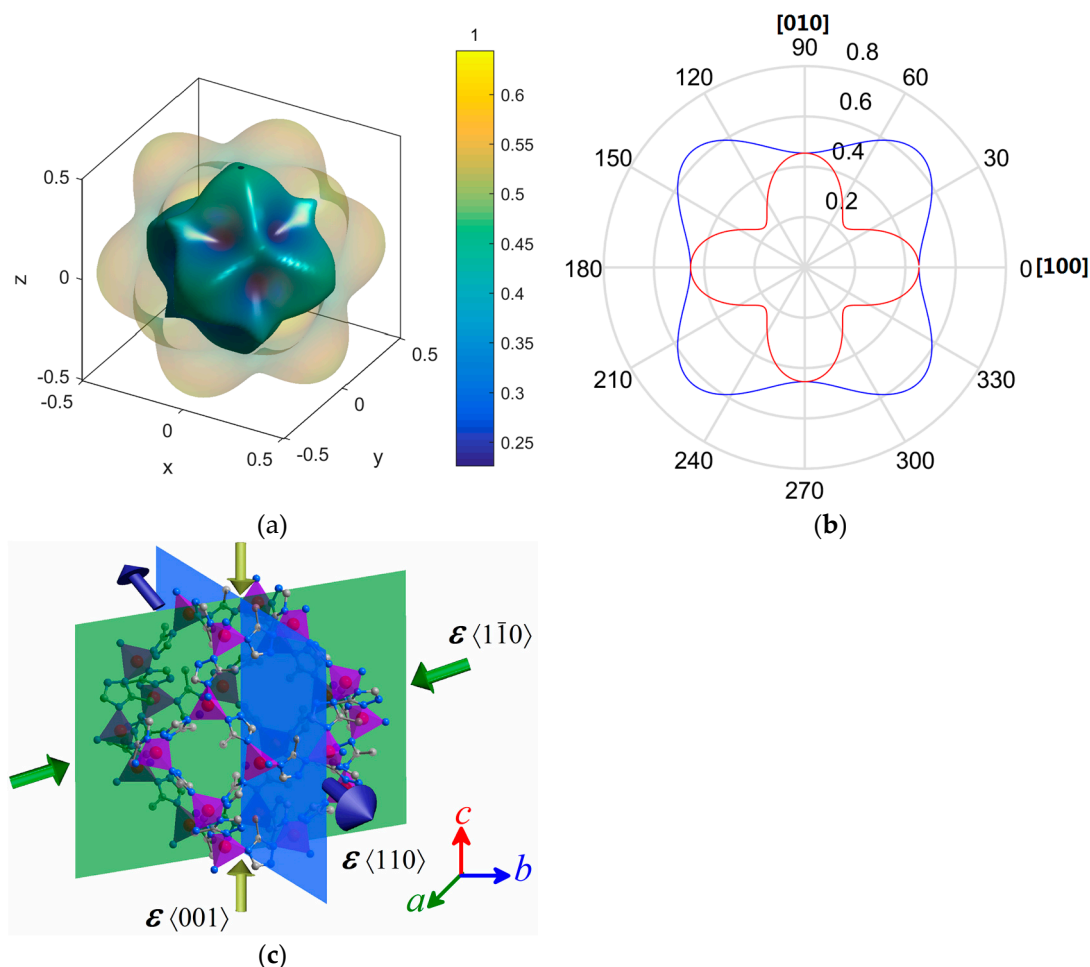
Figure 5. Poisson's ratio (ν) representation surfaces. (**a**) and 3D (**b**) 2D surface based on the calculational C_{ij} and corresponding polar plots obtained via projections through the origin and down the *c* axis, showing the positions of maximum and minimum modulus. (**c**) Axial and accompanying lateral directions that generate the positive ν_{max} and ν_{min}. Blue arrows represent the directions of loading, green and yellow arrows indicate contraction.

We finally focus on the bulk modulus (*B*), which represents the resistance of a material against hydrostatic stress. The *B* value derived from first-principle calculated elastic constants for MAF-7 is 10.29 GPa, indicating its stiffer character than ZIF-8 (theoretical values 9.23 GPa). To further demonstrate higher volume modulus from experimental view point, the high-pressure synchrotron X-ray powder diffraction experiments were performed. As shown in Figure 6, the diffraction peaks move to high angle direction with increasing pressure from 0 to 3.755 GPa, indicating the pressure-induced contraction of the framework. It is worth mentioning that no phase-transition occurs in MAF-7 in the whole pressure range, manifesting its higher stability to resist hydrostatic pressure than ZIF-8 with (phase transition about 0.34 GPa) [13]. The function of unit cell volume and lattice parameter *a* with respect to pressures (shown in Figure 7) were fitted using the second-order Birch-Murnaghan equation, and the obtained bulk modulus is 10.8(15) GPa, in excellent agreement with the calculated value (10.29 GPa). As expected, the experimental *B* value of MAF-7 is significantly larger than that of ZIF-8 (6.52(35) GPa), which further ascertains the high mechanical strength of MAF-7.
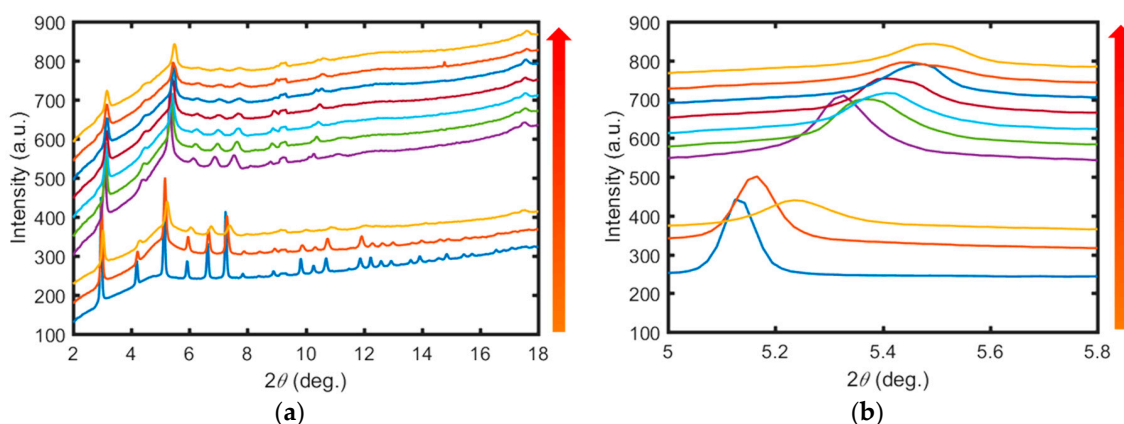
Figure 6. The representative synchrotron powder diffraction patterns of MAF-7 at 0, 0.177, 0.460, 0.862, 1.454, 1.848, 2.244, 2.829, 3.313, and 3.755 GPa, respectively. (**a**) Pressure increases from the bottom (0 GPa) to the top (3.755 GPa); and (**b**) right shift of the characteristic peak (112) with increasing pressure.
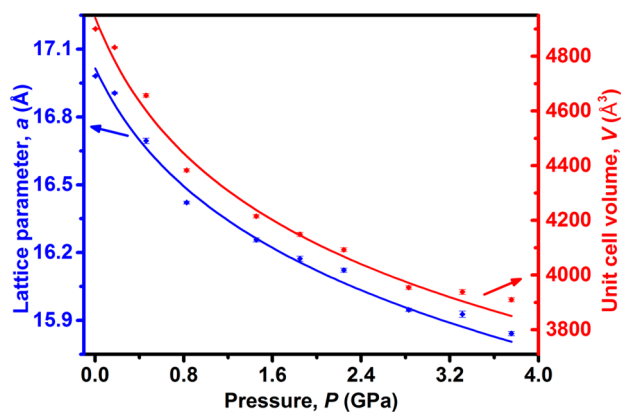
Figure 7. Pressure-dependent unit cell volume (*V*, blue) and lattice parameter (*a*, red). The experimental data are shown with error bars, and the red and blue lines indicate the second-order Birch-Murnaghan fits derived from a PASCAL program [25].

3. Materials and Methods

3.1. Synthesis of MAF-7

All chemicals and solvents were of reagent grade and used as received. Single crystals of $Zn(mtz)_2$ were prepared by slow evaporation from a clear aqueous ammonia solutions according to the method of Chen et al. [16] In the procedure, 0.084 g Hmtz (Aladdin) and 0.198 g $Zn(NO_3)_2 \cdot 6H_2O$ (Alfa Aesar) were dissolved in 10 mL aqueous ammonia solutions (25%) (Sinopham Chemical Reagent Co., Ltd., Shanghai, China). The colorless crystal have precipitated from liquid after a few days. Phase identification of a ground bulk sample was confirmed by X-ray powder diffraction (see ESI).

3.2. First-Principles Calculations

The first-principles elastic constant calculations were performed by CASTEP [26,27], a total energy package based on plane-wave pseudopotential density functional theory (DFT) [28]. The functionals developed by Perdew Burke and Ernzerhof (PBE) [29] in generalized gradient approximation (GGA) form [30] were adopted to describe the exchange–correlation energy. To account for the long-range dispersion interactions, the dispersion correction in DFT + D2 form developed by Grimme [31] was included in the calculation. Optimized ultrasoft pseudopotentials were adopted to model the effective interaction between the valence electrons and atom cores [32], which allow us to adopt a relatively

small plane-wave basis set without compromising the computational accuracy. The kinetic energy cutoff of 400 eV and the Monkhorst–Pack [33] k-point mesh spanning less than 0.03 Å^{-1} were chosen.

Before the elastic constant calculation, the crystal structure with no solvent molecules at 0 GPa was firstly optimized using the Broyden–Fletcher–Goldfarb–Shanno (BFGS) [34] minimization scheme, with the convergence criteria for energy, maximum force, maximum stress and maximum displacement set to 10^{-5} eV per atom, 0.03 eV, 0.05 GPa and 0.001 Å, respectively. Based on the optimized crystal structure, the elastic constants were calculated by the finite-strain method [35], in which the components of the elastic constant tensor were determined by the second-order derivative of energy with respect to specific strain and the maximum strain amplitude and the number of steps for each strain were set as 0.003 and three steps, respectively. After obtaining the calculated elastic constants, the analyses of Young's modulus, shear modulus and Poisson's ratio were performed using the ElAM program [21].

3.3. High-Pressure Synchrotron X-ray Powder Diffraction

The high-pressure experiments were performed on the 4W2 beam line of Beijing Synchrotron Radiation Facility with wavelength of the X-ray beam is 0.61992 Å. The gasket (300 μm in thickness) of the pre-indented stainless steel (T301) was placed on the systematic diamond anvil cells (DACs) (a culet diameter of 400 μm). The ground bulk samples were loaded in a cylindrical hole (about 150 μm in diameter), together with a few ruby chips for pressure calibration and a few drops of silicon oil used to act as pressure-transmitting medium for surrounding the samples and ensuring the uniform application of pressure. The required pressures were obtained by manually turning screws and the internal pressures were determined from measuring the shift of ruby luminescence [36]. The data were refined by using the Topas program [37].

3.4. Nanoindentation Methodology of Single Crystals

Nanoindentation experiments were performed under ambient conditions by employing a Hysitron TI 750 Ubi Triboindenter (Hysitron Corp., Minneapolis, MN, USA) in the continuous stiffness measurement mode [38]. A non-desolvated single crystal was first selected by well-defined regular dodecahedron shapes and, after face indexing, was confirmed by single-crystal X-ray diffraction using an Oxford Diffraction Rigaku XtaLAB mini^{TM} diffractometer (Rigaku Oxford Diffraction Ltd., Oxford, UK) with Mo-Kα radiation (λ = 0.70173 Å) at 300 K. Since any natural crystal facets were equivalent to the facet {110}, we had to polish off a certain natural facet to obtain an artificial facet (100). Crystals with {100} and {110}-oriented facets were then cold-mounted in epoxy resin and were carefully ground with emery paper up to 4000 grit, and polished with increasingly fine diamond suspensions to minimize surface roughness [15,22]. Accordingly, the indenter were aligned normal to the (100) and (110) crystal facets with a maximum surface penetration depth of 1200 nm [39]. The loading/unloading rates and the hold time at peak load, respectively, were maintained at 5000 μN s^{-1} and 30 s. A fused silica standard with an elastic modulus of 72 GPa and hardness of 9 GPa was used for calibration. Young's modulus (E_s) and indentation hardness (H) of the MAF-7 crystals were obtained from the *P-h* plots using the standard Oliver-Pharr method [40,41].

4. Conclusions

In summary, the elastic properties of MAF-7 were studied by first-principles calculation and experiment. Our results revealed that the elastic constant components of MAF-7 are about 5.0–73.3% higher than those of its isomorphous ZIF-8. Further analysis demonstrates that the elastic modulus, shear modulus and Poisson's ratio values of MAF-7 are about 3.4% to 20.1%, 3.2% to 20.6% and −30.3% to 12.3% larger than those of ZIF-8, respectively. The remarkable enhancement of mechanical stiffness from MAF-7 to ZIF-8 mainly originates from the electron-donating effect of the additional nitrogen atom in the triazolate ligand. Moreover, the underlying reasons of the anisotropic difference in each property were discussed from a viewpoint of framework structure. Furthermore, the calculated high

mechanical strength of MAF-7 is verified by nanoindentation and high-pressure X-ray diffraction experiment, indicating the reliability of our first principle calculations. We believe this study further deepens the understanding of mechanical properties of zeolitic azolate frameworks, and is informative for the exploration of MOF mechanics in general.

Supplementary Materials: The following are available online at www.mdpi.com/2073-4352/7/4/99/s1, Figure S1: The powder X-ray diffraction (PXRD) spectra of MAF-7 refined by Le Bail method. The black and red symbols, and the purple continuous lines are experimental, calculated, and difference profiles, respectively, and the vertical markers indicate the allowed Bragg reflections. Rp = 5.0%, Rwp = 7.4% and GOF = 4.598; Table S1: Lattice parameters and unit cell volume of MAF-7 at various pressure (GPa).

Author Contributions: Wei Li, Rong Wu, Zheshuai Lin and Guoqiang Feng conceived and designed the project; Xingxing Jiang performed the density functional theory calculations; Hongqiang Gao and Wenjuan Wei performed the experiments and analyzed the data; Hongqiang Gao and Wenjuan Wei wrote the paper under the supervision of Wei Li. All authors contributed to discussion of the results and reviewed the manuscript.

Conflicts of Interest: The authors declare no conflicts of interest.

References

1. Li, W.; Wang, Z.; Deschler, F.; Gao, S.; Friend, R.H.; Cheetham, A.K. Chemically diverse and multifunctional hybrid organic–inorganic perovskites. *Nat. Rev. Mater.* **2017**, 16099. [CrossRef]

2. Deng, H.; Doonan, C.J.; Furukawa, H.; Ferreira, R.B.; Towne, J.; Knobler, C.B.; Wang, B.; Yaghi, O.M. Multiple functional groups of varying ratios in metal-organic frameworks. *Science* **2010**, *327*, 846–850. [CrossRef] [PubMed]

3. Fukushima, T.; Horike, S.; Inubushi, Y.; Nakagawa, K.; Kubota, Y.; Takata, M.; Kitagawa, S. Solid Solutions of Soft Porous Coordination Polymers: Fine-Tuning of Gas Adsorption Properties. *Angew. Chem. Int. Ed.* **2010**, *49*, 4820–4824. [CrossRef] [PubMed]

4. Tanaka, D.; Higuchi, M.; Horike, S.; Matsuda, R.; Kinoshita, Y.; Yanai, N.; Kitagawa, S. Storage and Sorption Properties of Acetylene in Jungle-Gym-Like Open Frameworks. *Chem. Asian J.* **2008**, *3*, 1343–1349. [CrossRef] [PubMed]

5. Kleist, W.; Jutz, F.; Maciejewski, M.; Baiker, A. Mixed-Linker Metal-Organic Frameworks as Catalysts for the Synthesis of Propylene Carbonate from Propylene Oxide and CO_2. *Eur. J. Inorg. Chem.* **2009**, *2009*, 3552–3561. [CrossRef]

6. Cheetham, A.K.; Rao, C.N.R.; Feller, R.K. Structural diversity and chemical trends in hybrid inorganic–organic framework materials. *Chem. Commun.* **2006**, 4780–4795. [CrossRef]

7. Taylor-Pashow, K.M.; Rocca, J.D.; Xie, Z.; Tran, S.; Lin, W. Postsynthetic modifications of iron-carboxylate nanoscale metal-organic frameworks for imaging and drug delivery. *J. Am. Chem. Soc.* **2009**, *131*, 14261–14263. [CrossRef] [PubMed]

8. Li, W.; Kiran, M.S.R.N.; Manson, J.L.; Schlueter, J.A.; Thirumurugan, A.; Ramamurty, U.; Cheetham, A.K. Mechanical properties of a metal–organic framework containing hydrogen-bonded bifluoride linkers. *Chem. Commun.* **2013**, *49*, 4471–4473. [CrossRef] [PubMed]

9. Sun, S.; Henke, S.; Wharmby, M.T.; Yeung, H.H.M.; Li, W.; Cheetham, A.K. Mechanical Properties of a Calcium Dietary Supplement, Calcium Fumarate Trihydrate. *Inorg. Chem.* **2015**, *54*, 11186–11192. [CrossRef] [PubMed]

10. Zhang, Z.; Jiang, X.; Feng, G.; Lin, Z.; Hu, B.; Li, W. Mechanical properties and negative thermal expansion of a dense rare earth formate framework. *J. Solid State Chem.* **2016**, *233*, 289–293. [CrossRef]

11. Park, K.S.; Ni, Z.; Cote, A.P.; Choi, J.Y.; Huang, R.; Uribe-Romo, F.J.; Chae, H.K.; O'Keeffe, M.; Yaghi, O.M. Exceptional chemical and thermal stability of zeolitic imidazolate frameworks. *Proc. Natl. Acad. Sci. USA* **2006**, *103*, 10186–10191. [CrossRef] [PubMed]

12. Moggach, S.A.; Bennett, T.D.; Cheetham, A.K. The Effect of Pressure on ZIF-8: Increasing Pore Size with Pressure and the Formation of a High-Pressure Phase at 1.47 GPa. *Angew. Chem.* **2009**, *121*, 7221–7223. [CrossRef]

13. Chapman, K.W.; Halder, G.J.; Chupas, P.J. Pressure-induced amorphization and porosity modification in a metal-organic framework. *J. Am. Chem. Soc.* **2009**, *131*, 17546–17547. [CrossRef] [PubMed]

14. Tan, J.C.; Bennett, T.D.; Cheetham, A.K. Chemical structure, network topology, and porosity effects on the mechanical properties of Zeolitic Imidazolate Frameworks. *Proc. Natl Acad. Sci. USA* **2010**, *107*, 9938–9943. [CrossRef] [PubMed]

15. Tan, J.C.; Civalleri, B.; Lin, C.C.; Valenzano, L.; Galvelis, R.; Chen, P.F.; Bennett, T.D.; Mellot-Draznieks, C.; Zicovich-Wilson, C.M.; Cheetham, A.K. Exceptionally low shear modulus in a prototypical imidazole-based metal-organic framework. *Phys. Rev. Lett.* **2012**, *108*, 095502. [CrossRef] [PubMed]

16. Zhang, J.P.; Zhu, A.X.; Lin, R.B.; Qi, X.L.; Chen, X.M. Pore Surface Tailored SOD-Type Metal-Organic Zeolites. *Adv. Mater.* **2011**, *23*, 1268–1271. [CrossRef] [PubMed]

17. Zhu, A.X.; Lin, R.B.; Qi, X.L.; Liu, Y.; Lin, Y.Y.; Zhang, J.P.; Chen, X.M. Zeolitic metal azolate frameworks (MAFs) from $ZnO/Zn(OH)_2$ and monoalkyl-substituted imidazoles and 1,2,4-triazoles: Efficient syntheses and properties. *Microporous Mesoporous Mater.* **2012**, *157*, 42–49. [CrossRef]

18. Nye, J.F. *Physical Properties of Crystals*; Clarendon Press: Oxford, UK, 1985; p. 142.

19. Grimvall, G. *Thermophysical Properties of Materials*; Elsevier: Amsterdam, The Netherlands, 1999.

20. Feng, J. Mechanical properties of hybrid organic-inorganic $CH_3NH_3BX_3$ (B = Sn, Pb; X = Br, I) perovskites for solar cell absorbers. *APL Mater.* **2014**, *2*, 081801. [CrossRef]

21. Marmier, A.; Lethbridge, Z.A.; Walton, R.I.; Smith, C.W.; Parker, S.C.; Evans, K.E. ElAM: A computer program for the analysis and representation of anisotropic elastic properties. *Comput. Phys. Commun.* **2010**, *181*, 2102–2115. [CrossRef]

22. Li, W.; Barton, P.T.; Kiran, M.S.R.N.; Burwood, R.P.; Ramamurty, U.; Cheetham, A.K. Magnetic and Mechanical Anisotropy in a Manganese 2-Methylsuccinate Framework Structure. *Chemistry* **2011**, *17*, 12429–12436. [CrossRef] [PubMed]

23. Feng, G.; Jiang, X.; Wei, W.; Gong, P.; Kang, L.; Li, Z.; Li, Y.; Li, X.; Wu, X.; Lin, Z.; et al. High pressure behaviour and elastic properties of a dense inorganic–organic framework. *Dalton Trans.* **2016**, *45*, 4303–4308. [CrossRef] [PubMed]

24. Lethbridge, Z.A.; Walton, R.I.; Marmier, A.S.; Smith, C.W.; Evans, K. Elastic anisotropy and extreme Poisson's ratios in single crystals. *Acta Mater.* **2010**, *58*, 6444–6451. [CrossRef]

25. Cliffe, M.J.; Goodwin, A.L. PASCal: A principal axis strain calculator for thermal expansion and compressibility determination. *J. Appl. Cryst.* **2012**, *45*, 1321–1329. [CrossRef]

26. Clark, S.J.; Segall, M.D.; Pickard, C.J.; Hasnip, P.J.; Probert, M.I.; Refson, K.; Payne, M.C. First principles methods using CASTEP. *Z. Krist.* **2005**, *220*, 567–570. [CrossRef]

27. Payne, M.C.; Teter, M.P.; Allan, D.C.; Arias, T.A.; Joannopoulos, J.D. Iterative minimization techniques for ab initio total-energy calculations: Molecular dynamics and conjugate gradients. *Rev. Mod. Phys.* **1992**, *64*, 1045. [CrossRef]

28. Kohn, W.; Sham, L.J. Self-consistent equations including exchange and correlation effects. *Phys. Rev.* **1965**, *140*, A1133. [CrossRef]

29. Perdew, J.P.; Burke, K.; Ernzerhof, M. Generalized gradient approximation made simple. *Phys. Rev. Lett.* **1996**, *77*, 3865. [CrossRef] [PubMed]

30. Perdew, J.P.; Wang, Y. Pair-distribution function and its coupling-constant average for the spin-polarized electron gas. *Phys. Rev. B* **1992**, *46*, 12947. [CrossRef]

31. Grimme, S. Semiempirical GGA-type density functional constructed with a long-range dispersion correction. *J. Comput. Chem.* **2006**, *27*, 1787–1799. [CrossRef] [PubMed]

32. Sanchez-Portal, D.; Artacho, E.; Soler, J.M. Projection of plane-wave calculations into atomic orbitals. *Solid State Commun.* **1995**, *95*, 685–690. [CrossRef]

33. Monkhorst, H.J.; Pack, J.D. Special points for Brillouin-zone integrations. *Phys. Rev. B* **1976**, *13*, 5188. [CrossRef]

34. Pfrommer, B.G.; Côté, M.; Louie, S.G.; Cohen, M.L. Relaxation of crystals with the quasi-Newton method. *J. Comput. Phys.* **1997**, *131*, 233–240. [CrossRef]

35. Deyirmenjian, V.B.; Heine, V.; Payne, M.C.; Milman, V.; Lynden-Bell, R.M.; Finnis, M.W. Ab initio atomistic simulation of the strength of defective aluminum and tests of empirical force models. *Phys. Rev. B* **1995**, *52*, 15191. [CrossRef]

36. Mao, H.K.; Xu, J.A.; Bell, P.M. Calibration of the ruby pressure gauge to 800 kbar under quasi-hydrostatic conditions. *J. Geophys. Res.* **1986**, *91*, 4673–4676. [CrossRef]

37. Coelho, A. *TOPAS-Academic v5*, Coehlo Software: Brisbane, Australia, 2013.

38. Gao, H.; Wei, W.; Li, Y.; Wu, R.; Feng, G.; Li, W. Uniaxial Negative Thermal Expansion and Mechanical Properties of a Zinc-Formate Framework. *Materials* **2017**, *10*, 151. [CrossRef]

39. Li, W.; Thirumurugan, A.; Barton, P.T.; Lin, Z.; Henke, S.; Yeung, H.H.M.; Wharmby, M.T.; Bithell, E.G.; Howard, C.J.; Cheetham, A.K.; et al. Mechanical tunability via hydrogen bonding in metal–organic frameworks with the perovskite architecture. *J. Am. Chem. Soc.* **2014**, *136*, 7801–7804. [CrossRef] [PubMed]

40. Oliver, W.C.; Pharr, G.M. An improved technique for determining hardness and elastic modulus using load and displacement sensing indentation experiments. *J. Mater. Res.* **1992**, *7*, 1564–1583. [CrossRef]

41. Oliver, W.C.; Pharr, G.M. Measurement of hardness and elastic modulus by instrumented indentation: Advances in understanding and refinements to methodology. *J. Mater. Res.* **2004**, *19*, 3–20. [CrossRef]